



## Article

# Semantic Segmentation Model for Wide-Area Coseismic Landslide Extraction Based on Embedded Multichannel Spectral–Topographic Feature Fusion: A Case Study of the Jiuzhaigou Ms7.0 Earthquake in Sichuan, China

Xiangxiang Zheng <sup>1,2,3</sup> , Lingyi Han <sup>3</sup> , Guojin He <sup>1,2,4,5,\*</sup>, Ning Wang <sup>3</sup>, Guizhou Wang <sup>1,2,4,5</sup> and Lei Feng <sup>3</sup>

<sup>1</sup> Aerospace Information Research Institute, Chinese Academy of Sciences, Beijing 100094, China

<sup>2</sup> University of Chinese Academy of Sciences, Beijing 100049, China

<sup>3</sup> China Aero Geophysical Survey & Remote Sensing Center for Natural Resources, Beijing 100083, China

<sup>4</sup> Key Laboratory of Earth Observation Hainan Province, Sanya 572029, China

<sup>5</sup> Sanya Institute of Remote Sensing, Sanya 572029, China

\* Correspondence: hegj@aircas.ac.cn

**Abstract:** The rapid and accurate extraction of wide-area coseismic landslide locations is critical in earthquake emergencies. At present, the extraction of coseismic landslides is mainly based on post-earthquake site investigation or the interpretation of human–computer interactions based on remote sensing images. However, the identification efficiency is low, which seriously delays the earthquake emergency response. On the basis of the available multisource and multiscale remote sensing data, numerous studies have been carried out on the methods of coseismic landslide extraction, such as pixel analysis, object-oriented analysis, change detection, and machine learning. However, the effectiveness of coseismic landslide extraction was low in wide areas with complex topographic and geomorphic backgrounds. Therefore, this paper offers a comprehensive study of the factors influencing coseismic landslides and researches rapid and accurate wide-area coseismic landslide extraction methods with multisource remote sensing and geoscience technology. These techniques include digital elevation modeling (DEM) and its derived slopes and aspects. An embedded multichannel spectral–topographic feature fusion model for coseismic landslide extraction based on DeepLab V3+ is proposed, and a knowledge-enhanced deep learning information extraction method integrating geological knowledge is formed. Using the Jiuzhaigou Ms7.0 earthquake (seismic intensity VIII) in Sichuan Province, China, a comparison of landslide extraction models and strategies is carried out. The results show that the model proposed in this paper achieves the best balance in the accuracy and efficiency of wide-area extractions. Using multiple feature data of coseismic landslides, the problem of mixed pixels is solved. The rate of the misidentification of landslides as clouds, snow, buildings, and roads is significantly lower than in other methods. The identified landslide boundaries are smoother and more accurate, and the connectivity is better. Compared with other methods, ours can more accurately eliminate landslides not triggered by the Jiuzhaigou earthquake. While using the image block strategy to ensure extraction efficiency, it also improves the extraction accuracy of wide-area coseismic landslides in complex backgrounds.

**Keywords:** coseismic landslide; feature fusion; remote sensing; DEM; deep learning; DeepLab V3+



**Citation:** Zheng, X.; Han, L.; He, G.; Wang, N.; Wang, G.; Feng, L. Semantic Segmentation Model for Wide-Area Coseismic Landslide Extraction Based on Embedded Multichannel Spectral–Topographic Feature Fusion: A Case Study of the Jiuzhaigou Ms7.0 Earthquake in Sichuan, China. *Remote Sens.* **2023**, *15*, 1084. <https://doi.org/10.3390/rs15041084>

Academic Editors: Kasturi Devi Kanniah, Jagannath Aryal and Dongping Ming

Received: 16 December 2022

Revised: 10 February 2023

Accepted: 13 February 2023

Published: 16 February 2023



**Copyright:** © 2023 by the authors. Licensee MDPI, Basel, Switzerland. This article is an open access article distributed under the terms and conditions of the Creative Commons Attribution (CC BY) license (<https://creativecommons.org/licenses/by/4.0/>).

## 1. Introduction

Affected by topography, geological structure, and other factors, destructive earthquakes (magnitude 4.7) often trigger a large number of landslides. The characteristics of coseismic landslides include wide distribution and extensive damage. The rapid assessment of landslide distribution after earthquakes can provide critical support for emergency rescue. Therefore, how to obtain coseismic landslide information quickly and accurately has

become the focus of effective earthquake emergency rescue and post-earthquake secondary disaster prevention.

Coseismic landslide extraction is mainly based on post-earthquake field investigation and the visual interpretation of remote sensing data, which combines spectral features, texture features, and professional knowledge and experience, and has high accuracy [1,2]. However, due to the lack of expert knowledge support, the extraction efficiency of wide-area earthquake landslides is low and cannot meet the timeline requirements of earthquake emergency response. Relevant research has been conducted over the years on accurate automatic or semiautomatic landslide extraction methods. Several have been developed according to the similarities and differences in the spatial and temporal characteristics, imaging mechanism, and scene adaptability of the available data sources. Progress has been closely related to the development of remote sensing technology, following different stages, such as pixel analysis for low- and medium-resolution remote sensing, machine learning for multiscale remote sensing, object-oriented methods for high-resolution remote sensing, and deep learning methods for multisource data.

Specifically, unsupervised and supervised classification methods, such as statistical regression, image transformation, and fuzzy C-means clustering, are mostly used to achieve pixel-scale landslide detection based on medium- and low-resolution remote sensing images and derived remote sensing indexes [3–16]. Different machine learning methods, such as artificial neural networks, support vector machines (SVM), and random forests, have been applied for landslide extraction based on medium- and high-resolution multiscale remote sensing [17–21]. In recent years, with the rapid development of high-resolution remote sensing technology [22], object-oriented analysis methods have become more widely used in landslide extraction research. Compared with medium- and low-resolution remote sensing, landslide identification can be more refined through high-resolution remote sensing. The object-oriented analysis method takes a homogeneous image of the object generated by image segmentation as the basic unit of analysis. It comprehensively uses the spectrum, texture, shape, context, and other characteristics of object segmentation to realize automatic landslide identification. Numerous object-oriented analysis methods based on multiscale segmentation, the level set algorithm, and other multi-feature combinations have been used based on high-resolution remote sensing images and airborne LiDAR data in different regions [4,23–53]. With the rapid development and extensive application of artificial intelligence in computer image recognition, more scholars are trying to extract landslides using semantic segmentation, unsupervised learning, and other deep learning models and migration learning methods based on multisource data [17,54–64].

In addition, when multitemporal remote sensing images of an earthquake area are obtained after an earthquake, change detection methods are used to identify coseismic landslides. Because of the synthetic aperture radar's (SAR) characteristics, such as its all-weather operation and fast response, research on landslide detection based on multitemporal SAR strength data and coherence changes has also been conducted [65–68]. However, their results differed due to the area, scatterer characteristics, and algorithm capability. Detection accuracy is still controversial, especially in low coherence areas [69].

Image spectral information can be used to quickly classify similar pixels into one category using pixel analysis [70]. However, because of the constraints of low and medium spatial resolution, the extraction accuracy is usually limited, and it is difficult to accurately identify landslides of different scales. The method does not consider the geometry, structure, texture, and other remote sensing characteristics of the target object [52], so the pixel analysis method is affected by interference from similar types of ground objects. Since it is difficult to distinguish ground objects with spectral characteristics similar to those of the landslide, such as bare soil, a river course, etc., the analysis suffers from missed and wrong classifications, which produces salt and pepper noise, reduced accuracy, and homogeneity of the classification results [2,70]. To overcome these problems, the object-oriented analysis for high-resolution images was subsequently widely adopted. This method improved the accuracy of landslide recognition by employing a combination of image segmentation and

classification rules for features such as the spectrum, texture, structure, and shape of the landslide in the image. However, because of the complexity of the data, this method often relies on human experience for adjusting the feature selection, setting classification rules, and determining the threshold of segmentation parameters, such as spectral weight, homogeneity factor, segmentation scale, etc. Thus, this method often results in high uncertainty, low automation, and poor timeliness during experiments [47,48,70].

The machine learning method for multiscale remote sensing relies on numerous landslide feature samples to realize landslide recognition. The research on object-oriented landslide recognition analysis and machine learning methods has greatly promoted the development of computer recognition technology. However, the computer recognition-based methods do not regard a landslide as a complex object within a specific geological environment; it uses middle- and low-level features, such as spectrum, texture, structure, etc., and lacks the ability to transfer the image processing and visual interpretation mode to the computer for automatic recognition. Thus, high-level semantic image information cannot be described accurately. Hence, the recognition accuracy and availability of this method are limited and it is still challenging to meet the requirements for its practical application [2].

Deep learning, such as semantic segmentation, object detection, etc., has been widely used in computer imaging in recent years. As a data-driven method, its essence is a mathematical model composed of multiple nonlinear functions. Its composite processing is a mathematical process that automatically obtains the characteristics of high-level functions through multiple low-level features. Nonlinear composite processing with multiple functions can be a more complex function correlation than manual fitting. It can extract more useful information related to landslide from low-value density data—deep-level abstract features—without manually designing high-level features. The cost of manual error in its operation is greatly reduced, and the recognition is efficient and accurate [70–72]. At present, the research on deep learning in remote sensing information extraction usually treats remote sensing images as natural pictures. It directly transfers the successful application of deep learning in natural pictures to remote sensing information extraction without considering how to integrate the scientific knowledge related to the research object with the deep learning model.

In summary, the summary of landslide remote sensing information extraction methods is shown in Figure 1. Therefore, this study carried out research on the embedded multi-channel spectral–topographic feature fusion method for extracting coseismic landslides. This research aimed to effectively integrate the optical image features and the geological condition data related to coseismic landslides into a deep learning model and establish a knowledge-enhanced deep learning model for the extraction of coseismic landslides in order to avoid the uncertainty of results caused by differences in coseismic landslide characteristics and reduce the subjectivity of coseismic landslide extraction using expert experience, thus improving the efficiency of extraction. This study will play a great role in pre-earthquake and post-earthquake assessment. It is embodied in two aspects: accuracy and efficiency. Specifically, through the methodology of this study, high-precision occurred landslide data can be provided as basic data before the earthquake, and high-precision coseismic landslide data can be provided quickly after the earthquake to assist emergency decision-making.

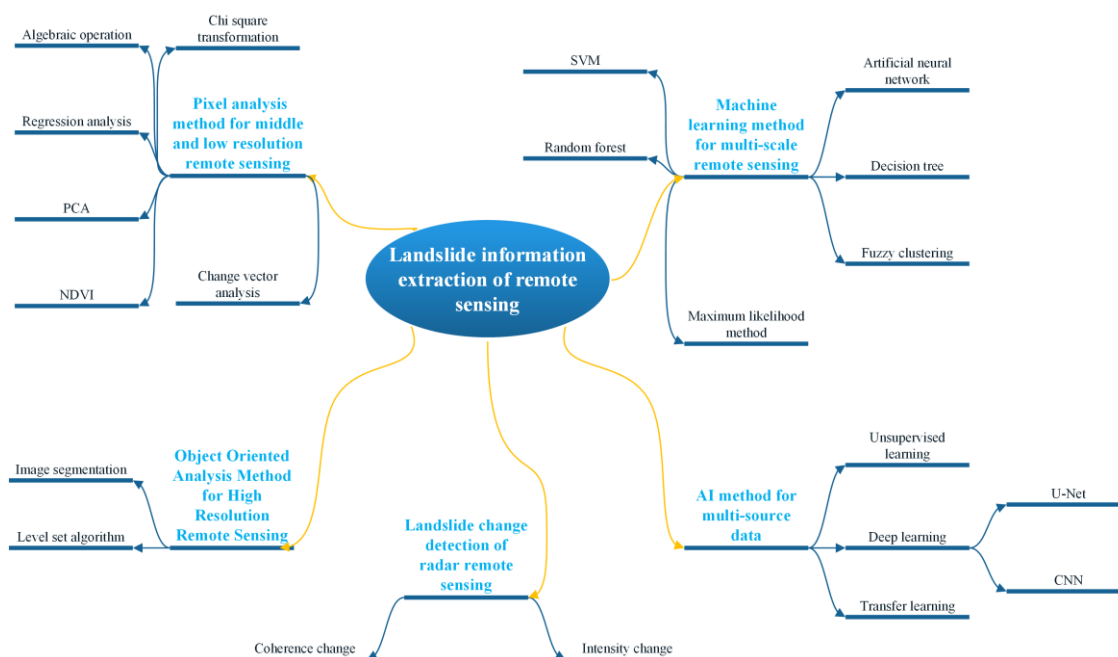


**Figure 1.** Summary of landslide remote sensing information extraction methods.

## 2. Methods

### 2.1. Research Technical Route

The research route for the rapid extraction of coseismic landslide information based on an embedded multichannel spectral–topographic feature fusion model is shown in Figure 2. The process includes multisource data acquisition, data processing, coseismic landslide cataloging and feature combination, sample output and preprocessing, model training, verification, and comparison.

- (1). Multisource data acquisition. Because optical remote sensing and digital elevation modeling (DEM) data are required for the extraction of coseismic landslides, it is necessary to obtain multisource time series optical remote sensing images and post-earthquake satellite stereo mapping data covering the study area. The pre- and post-earthquake multitemporal optical remote sensing images are mainly based on China’s land change survey, and the post-earthquake and stereo mapping satellite stereo image pair data are based on ZY-3 DLC data, which was acquired by the ZY-3 satellite belongs to the Ministry of Natural Resources, China.
- (2). Data processing. Data processing includes the synthesis of cloudless optical remote sensing images before and after earthquakes and the generation of DEM data after earthquakes. The former is based on pre- and post-earthquake multitemporal remote sensing images through the cloud mask and mosaic. The latter is based on the post-earthquake ZY-3 DLC data and is completed using the methods of “multi class image pair combined DSM extraction” and “median synthesis filtering”. The above work is completed using the flow data processing tools provided by PCI.
- (3). Coseismic landslide cataloging and feature combination. According to the data results obtained in (1) and (2), the remote sensing interpretation and cataloging of coseismic landslides are carried out using multitemporal and multisource remote sensing data. Simultaneously, the spectral band combination and topographic feature data, including optical remote sensing images, DEM, and its derived data are determined using consistent resampling, band registration, and combination methods to form a feature dataset.
- (4). Sample output and preprocessing. Sample size ( $256 \times 256$ ) and sample format (PASCAL format) are determined using the cataloging data and coseismic landslides feature dataset from (3) on the basis of the analysis of the spatial distribution, scale,

- and model input requirements. The sample data are formed containing label masks and feature data slices, and the radiation consistency and diversity of samples are improved through sample standardization and sample enhancement processing.
- (5). Multichannel spectral–topographic feature fusion model experiment. The sample data from (4) are randomly divided into the training set, test set, and verification set in a 6:3:1 proportion. Using a different number of channels, models, and backbone networks, a multichannel spectral–topographic feature fusion training and testing model for detecting the same earthquake landslide is obtained. Precision, mIou, F1 score, and other precision evaluation indicators are selected for comparative analysis of the results, and the embedded multichannel spectral–topographic feature fusion model proposed in this study is objectively evaluated.

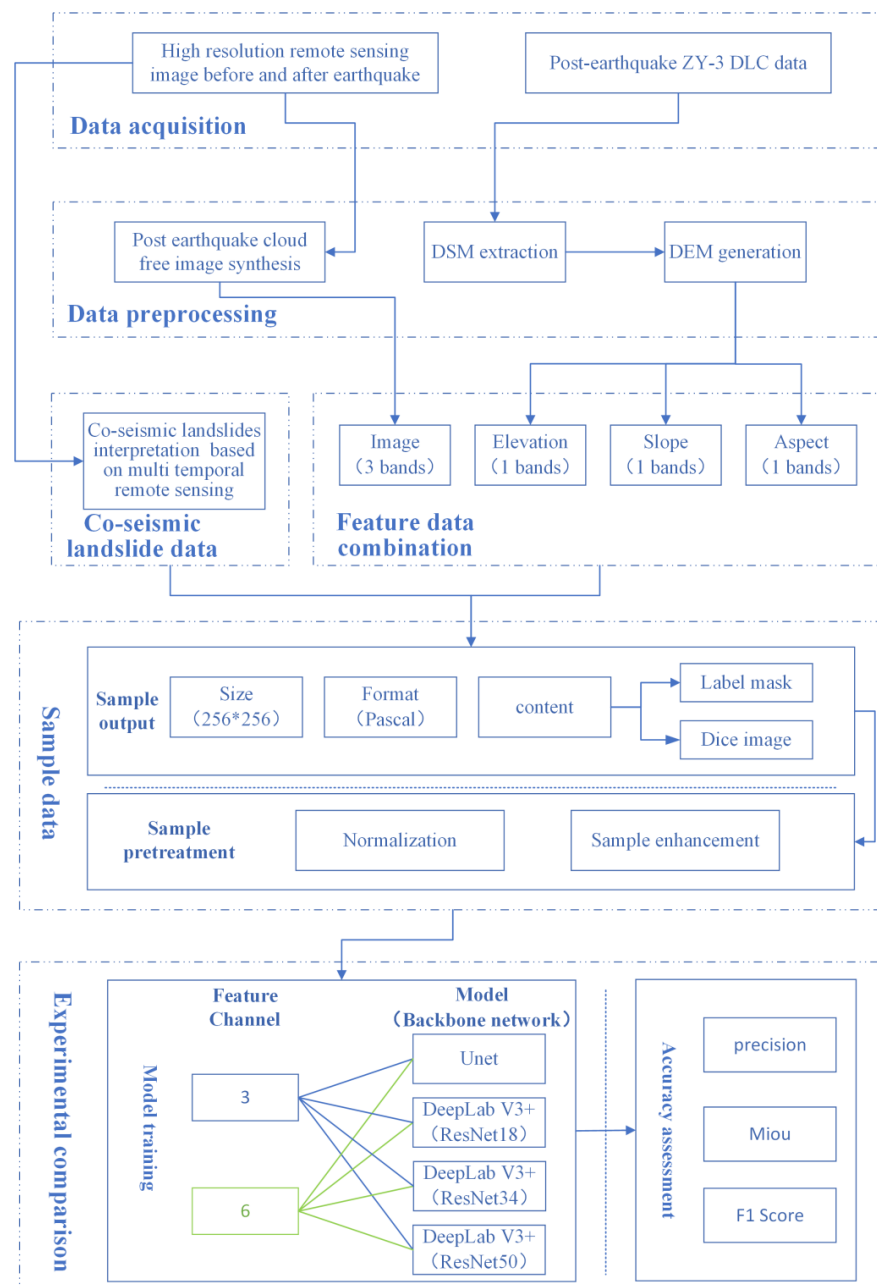
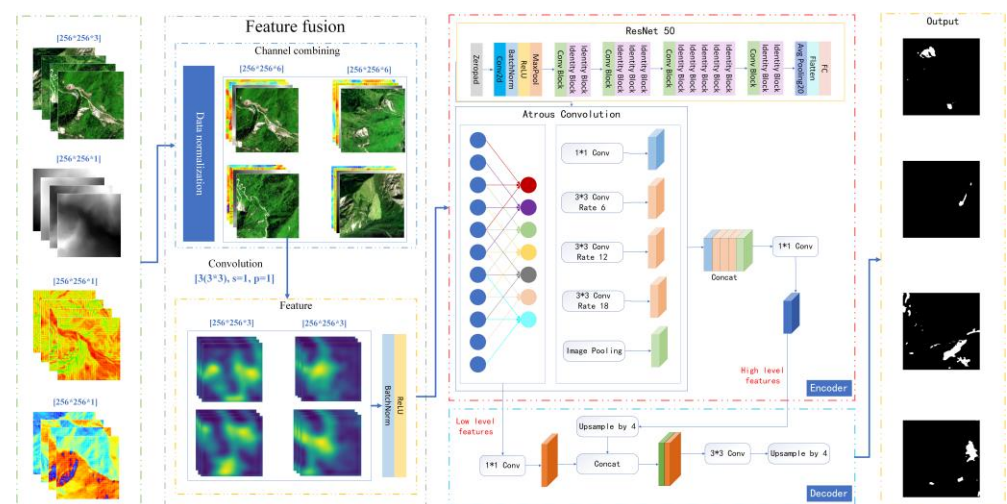


Figure 2. Research route.

## 2.2. Embedded Multichannel Spectral–Topographic Feature Fusion Model

Landslides are affected by many physical factors, including topography and geological conditions, as well as natural and human forces. Coseismic landslides are disasters associated with earthquakes. The micro geomorphic conditions of the hillside before the landslide are particularly important [49,73], especially the elevation, slope, and aspect of the natural hillside, which play an important role in triggering the coseismic landslide.

To fully use the features of the coseismic landslide in the optical remote sensing image and topography, this study proposes an embedded multichannel spectral–topographic feature fusion coseismic landslide extraction model based on DeepLab V3+. The model is constructed through the optimization and adjustment of the multichannel feature fusion and backbone network and is mainly composed of three parts: embedded multichannel feature fusion, ResNet with atrous convolution, and the encoder–decoder composed of atrous spatial pyramid pooling (ASPP). The encoder–decoder structure is consistent with the DeepLab V3+ model structure. The overall structure of the optimized and improved embedded extraction model is shown in Figure 3.



**Figure 3.** Overall architecture of embedded multichannel spectral–topographic feature fusion model based on DeepLab V3+.

### 2.2.1. Multichannel Spectral–Topographic Feature Fusion Input

To make full use of the multiple features affecting landslide extraction, such as images and topography, we carried out a targeted optimization and improvement of the conventional DeepLab V3+ model for natural images so that it could realize the integrated input of multiple features of the target object. The model input was optimized using data normalization and feature fusion.

Specifically, we first normalized the spectral–topographic features of each band according to the following formula:

$$(\text{PixValue} - \text{PixValue}_{\min}) / (\text{PixValue}_{\max} - \text{PixValue}_{\min}) \times 255 \quad (1)$$

Normalized multichannel feature data were then combined with the band combination method to form a multiband spectral–topographic feature dataset. To ensure that the multiband spectral–topographic data could be input to the DeepLab V3+ for feature learning, we added an embedded pre-convolution operation prior to the DeepLab V3+; we used three  $3 \times 3$  convolution kernels, the convolution operators with  $\text{string} = 1$ , and  $\text{padding} = 1$  to obtain a feature fusion dataset with channel 3 and constant size. The principle is shown in Figure 4.

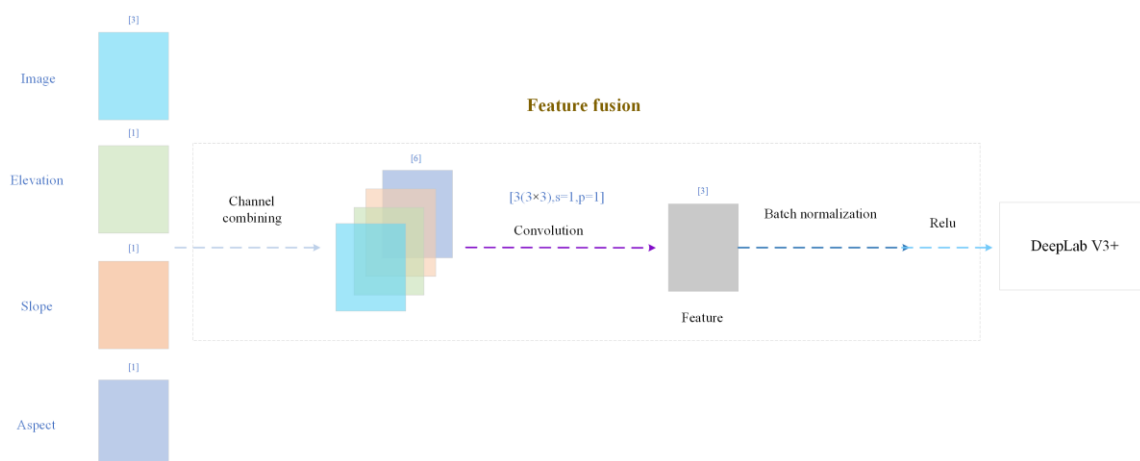


**Figure 4.** Feature fusion principle.

### 2.2.2. DeepLab V3+ Model

DeepLab V3+ combines the advantages of the spatial pyramid module and the encoder–decoder structure. On the one hand, the spatial pyramid module explores multiscale context information by using multi-sampling rate expansion convolution, multi-receiving field convolution, or pooling on the input features. On the other hand, DeepLab V3+ introduces the decoder module, which further integrates the low-level detail features with high-level semantic features. The encoder–decoder structure captures clearer object boundaries by gradually recovering spatial information and improving the accuracy of segmentation boundaries [74].

Specifically, the encoder of DeepLab V3+ comprises the atrous spatial pyramid pooling (ASPP) module and the backbone network. The atrous convolution is essential to the model because it reduces the downsampling rate while the receptive field can be guaranteed. The resulting feature map is not only rich in semantics but also relatively fine, and the original resolution can be directly restored through interpolation. By modifying the block behind the backbone network, the ASPP module replaces the lower sampling layer with atrous convolution and uses it at different rates to control the receptive field without changing the feature image size to extract multiscale information. ASPP uses multiple parallel atrous convolutions combined with image-level features (i.e., global average pooling). It can be seen from Figure 3 that the ASPP module mainly consists of a  $1 \times 1$  convolution layer, three  $3 \times 3$  atrous convolutions, and an image-pooling layer. The convolution layer can extract local features, and the image-pooling layer can extract global features.

Five different-scale features are fused using the concatenation method. After  $1 \times 1$  convolution, high-level semantic features are obtained. The structure of the decoder is relatively simple. First, the features obtained by the encoder are sampled four times using bilinear interpolation. The features are fused with the low-level features of the corresponding size in the encoder through the concatenation method. Next,  $3 \times 3$  convolution is used to further fuse the features, and, finally, bilinear interpolation is used to obtain a segmentation prediction of the same size as the original image. All upsamples in the decoder adopt the bilinear interpolation method.

DeepLab V3+ is a model of encoder–decoder architecture that uses the encoder as the downsampling module and DeepLab V3 to extract features. The decoder is an upsampling module that uses a simple but effective module to recover the boundary details of an object by interpolation and other methods and can use expansion convolution to control the resolution of a feature under the specified computing resources.

### 2.2.3. Backbone Network Selection

The backbone network of DeepLab V3+ can be any DCNN classification network. ResNet has been widely used in various feature extractions, and it is used in this study.

When the deep learning network has deeper layers, the theoretical expression ability will be stronger. However, when the CNN network reaches a certain depth, the classification performance will not improve, but will instead result in slower network convergence and lower accuracy. Even if the dataset is increased and the problem of overfitting is solved, the classification performance and accuracy will not improve. In response to the above problems, ref. [75] proposed a residual network to make the model easier to optimize by adjusting the model structure.

The stacked layer is called a block by the residual network. For a block, the function that can be fitted is  $F(x)$ . If the expected potential mapping is  $H(x)$ , instead of letting  $F(x)$  directly learn the potential mapping, it is better to learn the residual  $H(x) - x$ , that is,  $F(x) = H(x) - x$ , so that the original forward path becomes  $F(x) + x$ , and  $F(x) + x$  is used to fit  $H(x)$ . Compared with learning that  $F(x)$  is an identity map, it is easier to learn that  $F(x)$  is 0; the latter can be easily realized through L2 regularization. In this way, for redundant blocks, identity mapping can be obtained by  $F(x) \rightarrow 0$  with no performance degradation. A block composed of  $F(x) + x$  is called a residual block. As is shown in Figure 5, several similar residual blocks are connected in a series to form the ResNet [76].

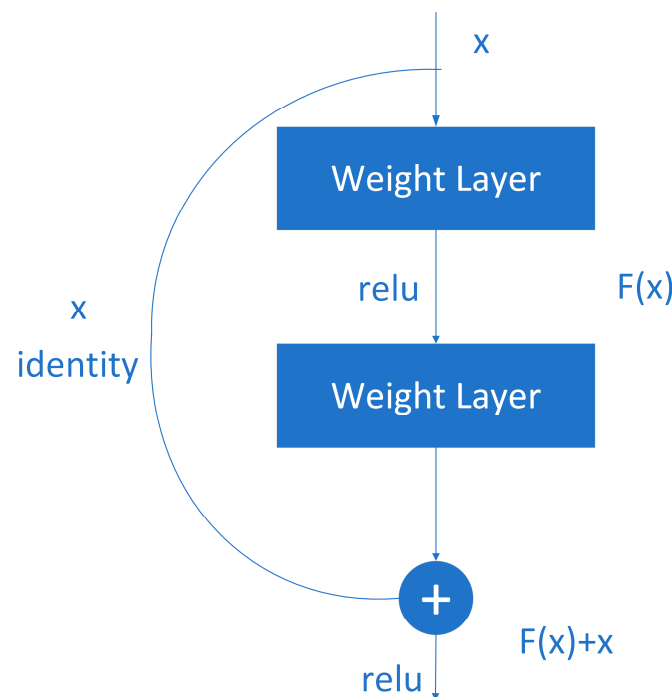


**Figure 5.** Residual block.

ResNet has five main networks with different depths: ResNet18, ResNet34, ResNet50, ResNet101, and Resnet152. These five networks are divided into five parts: Conv1\_x, Conv2\_x, Conv3\_x, Conv4\_x, and Conv5\_x. They are all built according to the above structure. The differences between networks are mainly due to the differences in block parameters and the number of intermediate convolutions [75]. ResNet18 and ResNet34 belong to small networks, and ResNet50, ResNet101, and ResNet152 belong to large networks. Reference [75] has compared the structure, parameters, accuracy, and computational complexity (FLOPs) of five networks. According to the results, with an increase in network depth, the computational complexity also increases, e.g., when the network depth is between 50 and 101 layers, the computational complexity increases from  $3.8 \times 10^9$  to  $7.6 \times 10^9$ . To balance the image segmentation effect and calculation efficiency of the model and realize the rapid and accurate extraction of coseismic landslide information after an earthquake, ResNet50 is preferred as the backbone network in terms of network layers

and calculation complexity. In the follow-up experiment, the model validation results for U-Net, ResNet18, ResNet34, and ResNet50 were compared and analyzed.

The ResNet50 network structure is shown in Figure 3 and will not be repeated here. The literature [76] shows the composition of two important basic blocks in the residual network structure, namely, the convolution block and the identity block, presented in Figure 6. The dimensions of the input and output of the convolution block are different and, therefore, cannot be connected in series; its role is to change the dimensions of the network. The identity block has the same input and output dimension, which can be concatenated to deepen the network.

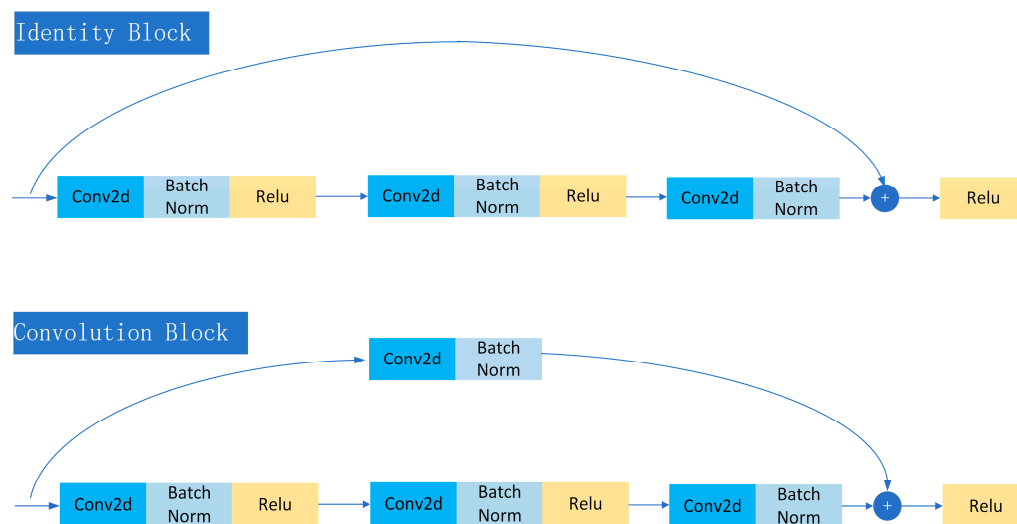


**Figure 6.** Two important basic blocks in the residual network structure.

### 3. Experiments

#### 3.1. Study Area

Landslides and other secondary earthquake disasters brought on by strong earthquakes have caused severe casualties and posed a serious challenge to timely emergency rescue response [77–83]. On 8 August 2017, a strong earthquake of Ms7.0 magnitude occurred in Jiuzhaigou County, Aba Prefecture, Sichuan Province, with a focal depth of 20 km. The epicenter elevation was more than 3500 m, and it was 35 km from Jiuzhaigou County and 210 km from Aba Prefecture. The Jiuzhaigou earthquake occurred in the transition area between the Qinghai Tibet Plateau and the Sichuan Basin, at the intersection area of the Huya fault at the east boundary of the Bayan Hara block and the Tazang fault at the east section of the East Kunlun fault zone. The topography varied, with the elevation decreasing from 4500 m to 1000 m west to east, and the slope was generally above 30°. The geomorphic features mainly included high mountains, deep valleys, slopes, and mountains. A topographic map of the study area is shown in Figure 7.

All strata in the study area are distributed. Among them, Cambrian and Ordovician systems are not completely developed and are only sporadically exposed. The late Paleozoic strata are relatively complete and are mainly Devonian, Carboniferous, and Permian. The Triassic strata of the Mesozoic era are the most widely distributed, lacking the Jurassic system and scattered in the Cretaceous system. The Cenozoic–Quaternary is less developed and scattered in basins, valleys, and gullies [77,78,84,85]. A basic geological map of the study area is as shown in Figure 8. Because of the area’s unique topographic and geomorphic makeup and its complex geological background, free conditions have developed at the front edge, with poor slope stability and susceptibility to landslide formation at the slope. In addition, because of the amplification effect of the peak acceleration generated by the ground motion on the seismic action and the degree of damage caused by the change in the rock mass and slope structure, this strong earthquake produced a large number of landslides and collapses.

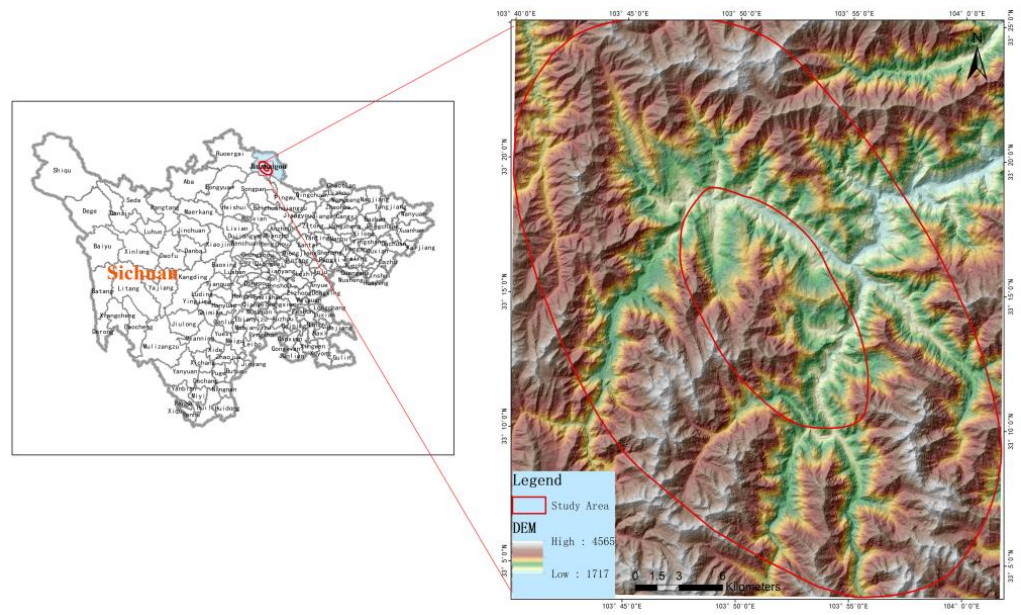


Figure 7. Topographic map of the study area.

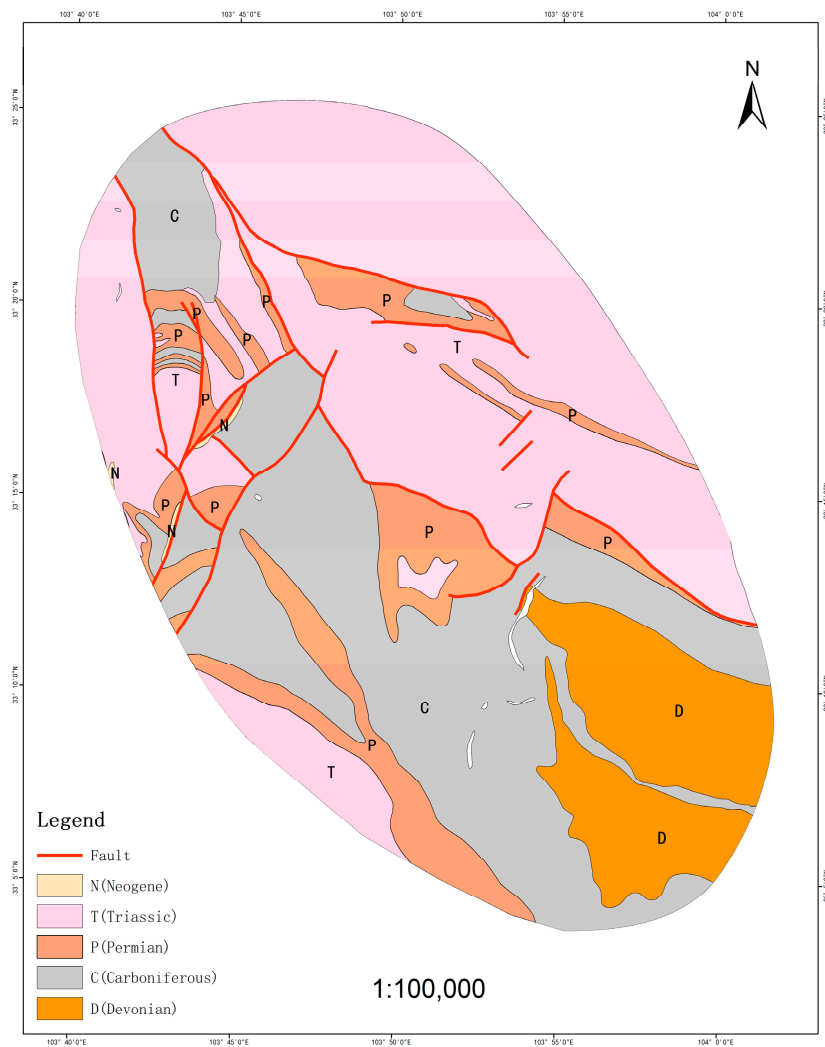


Figure 8. Basic geological map of the study area.

According to the literature [78], data on the Jiuzhaigou peak ground motion acceleration and seismic intensity released by the China Seismological Bureau and the interpretation results on the Jiuzhaigou earthquake coseismic landslides show that Jiuzhaigou earthquake-triggered landslides were essentially distributed in areas with seismic intensity greater than VIII, and almost all the interpretable seismic landslides occurred in areas with seismic acceleration greater than 0.15 g. Coseismic landslides in areas with seismic intensity greater than VIII accounted for about 80% of the total number of Jiuzhaigou earthquake-triggered landslides. Therefore, the area of the Jiuzhaigou earthquake identified by the China Seismological Bureau in which seismic intensity was greater than VIII is taken as the study area. This includes the IX degree area of Zhangzha Town, Jiuzhaigou County, Aba Tibetan, and Qiang Autonomous Prefecture, Sichuan Province, covering an area of 139 km<sup>2</sup>, and the VIII degree area of Zhangzha Town, Dalu Township, Heihe Township, Lingjiang Township, and Ma Hometown, Jiuzhaigou County, Aba Tibetan, and Qiang Autonomous Prefecture, Sichuan Province, covering an area of 778 km<sup>2</sup>. The total study area size is 917 km<sup>2</sup>.

### 3.2. Dataset

According to the research method determined in Section 2.1, this study collected multisource data, including pre- and post-earthquake multi temporal remote sensing data, post-earthquake ZY3 stereo mapping satellite data and its derived data, and seismic related data, as shown in Table 1. High-precision interpretations of coseismic landslides in the study area were obtained using the time series comparison method. DSM/DEM data extraction based on a stereo mapping satellite was also carried out to provide a timelier high-resolution DEM for the input of topographic features. A list of specific datasets used in this study is shown in Table 1.

**Table 1.** List of data used in the study.

Data Type	Spatial Resolution	Time	Data Source
Post-earthquake optical remote sensing image	5 m	After 8 August 2017	Ministry of Land and Resources, China
Pre-earthquake optical remote sensing image	2 m/5 m	Before 8 August 2017	Ministry of Land and Resources, China
ZY3 DLC stereo mapping satellite raw data	2.5 m	October 2017–January 2018	Land Satellite Remote Sensing Application Center, Ministry of Natural Resources, China
DEM extracted from ZY3 DLC data	5 m	October 2017–January 2018	Data processing
Slope	5 m	October 2017–January 2018	Data processing
Aspect	5 m	October 2017–January 2018	Data processing
Coseismic landslide cataloguing data based on pre-earthquake and post-earthquake multi temporal optical images	---	---	Human–computer interaction interpretation
Jiuzhaigou seismic intensity data	---	12 August 2017	China Seismological Bureau
Monitoring data of Jiuzhaigou Seismic Peak Acceleration Station	---	21:19:59, 8 August 2017	China Seismological Bureau

The cloud cover area in the image after the Jiuzhaigou earthquake is relatively large and had a certain impact on the integrity of the landslide interpretation. However, there is less cloud cover in the IX and VIII intensity areas, i.e., the study area, especially along the long axis of seismic intensity, as is shown in Figure 9. The image of the study area meets the needs of remote sensing interpretation of landslides triggered by this earthquake.

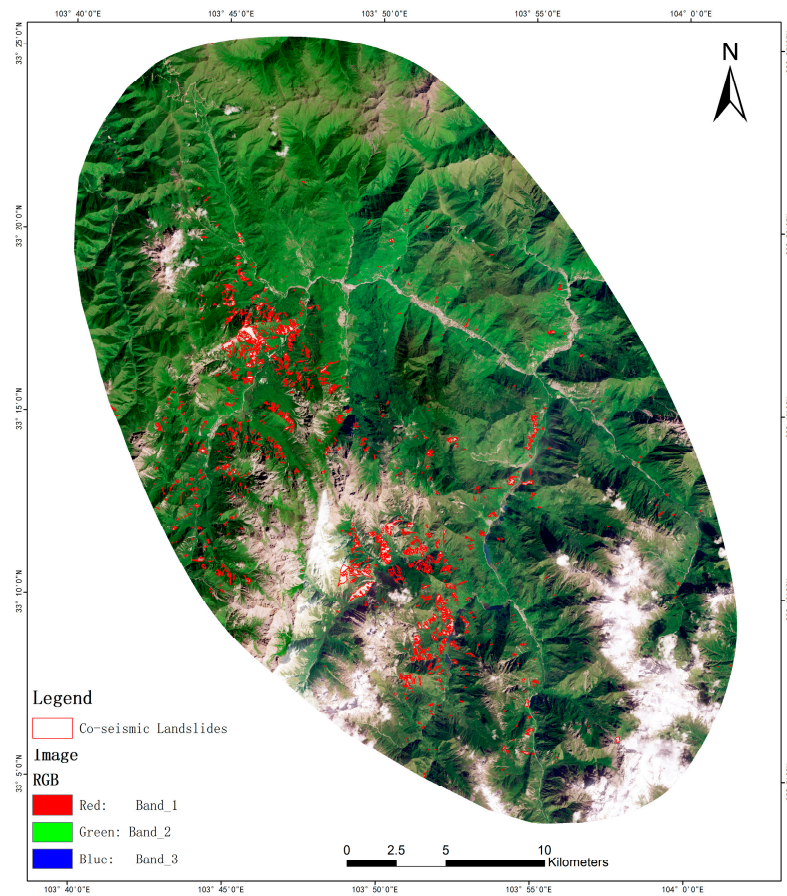


**Figure 9.** Distribution of coseismic landslides in the study area.

This study uses the method of comparison of remote sensing images acquired before and after the earthquake to determine whether the landslide was triggered by the Jiuzhaigou earthquake. If the landslide is present in the image taken before the Jiuzhaigou earthquake, and the shape of the image after the earthquake remains unchanged, then the landslide is considered to predate the Jiuzhaigou earthquake. If the landslide is not present in the image taken before the earthquake, or exists in the image before the earthquake but changes in those taken after the Jiuzhaigou earthquake, it is considered a Jiuzhaigou earthquake-triggered landslide. With this understanding, 937 Jiuzhaigou earthquake-triggered landslides were determined to have occurred in the study area. They were mainly small and medium-sized landslides distributed in strips along both sides of the extension line at the north end of the Huya fault, mostly along roads and valleys [78].

### 3.3. Evaluating Indicator

In order to quantitatively evaluate the performance of the models, this study used Precision, Recall, F1 Score, and mIoU to compare the recognition accuracy of the different models.

Precision refers to the proportion of the predicted positive and true positive cases, which accounts for all the predicted positive cases. It mainly refers to the number of targets that were accurately identified. The calculation formula is as follows:

$$\text{Precision} = \text{TP} / (\text{TP} + \text{FP}) \quad (2)$$

Recall refers to the proportion of the parts predicted as positive and actually positive. It accounts for the proportion of all positive cases, indicating how many correct targets have been identified. The calculation formula is as follows:

$$\text{Recall} = \text{TP}/(\text{TP} + \text{FN}) \quad (3)$$

The F1 Score is the harmonic average of the accuracy rate and recall rate. It combines the accuracy and recall rate results and belongs to a comprehensive evaluation index. When the F1 value is high, it indicates that the method is effective. The calculation formula is as follows:

$$\text{F1 - Score} = 2/((1/\text{Precision}) + (1/\text{Recall})) = 2\text{TP}/(\text{FP} + 2\text{TP} + \text{FN}) \quad (4)$$

where mIoU calculates the ratio of the intersection and union of the “predicted border” and “real border”. In image segmentation, this index is usually lower than calculating the correct classification probability of each pixel directly and is more sensitive to error classification. FP is a false positive example, FN is a false negative example, TP is a real example, and TN is a true negative example. Table 2 gives the relevant definitions.

**Table 2.** Relevant definitions.

	Predictive Value = 1	Predictive Value = 0
True Value = 1	TP	FN
True Value = 0	FP	TN

#### 4. Result

To fully understand the impact of feature input, model selection, and training strategy on landslide identification, different semantic segmentation models were trained and tested according to the research methods presented in Section 2. All involved DNNs were implemented with an NVIDIA Tesla V100 graphics processing unit (GPU), Compute Unified Device Architecture (CUDA) 10.1, and CUDA DNN library (CuDNN) 10.1.

The feature input of this study included the single-feature optical remote sensing image and multichannel spectral–topographic fusion features. The model was selected as U-Net and DeepLab V3+ composed of different backbone networks. The training strategy was based on the convergence of the loss function of the training set and the verification set during the model training process, and the parameters were constantly optimized and adjusted to avoid overfitting and underfitting and obtain a model with strong generalization ability.

Table 3 lists the experiments carried out with the different models. According to the differences in the number of input features and considering the differences between the models (backbone network) and the training strategies, the experiments carried out were uniformly numbered for subsequent comparative analysis. Among them, 1-1 to 1-5 are single-image feature inputs (three-band input features), and 2-1 to 2-5 are multichannel spectral–topographic feature fusion inputs (six-band input features).

Table 3 gives the quantitative accuracy evaluation of the different models for all the experiments. The evaluation indicators are the Precision, mIoU, Recall, and F1 Scores discussed in Section 3.3.

It can be seen from the precision evaluation results in Table 4 and Figure 10 that under the same feature input conditions, the precision evaluation index values of DeepLab V3+ are higher than those of U-Net. For DeepLab V3+, the accuracy evaluation index is improved partially with the increase in the depth of the backbone network. The increase in the number of training epochs also improves the accuracy of the model to a certain extent when the model continues to converge. Compared with the single-feature input of an optical image, the increase in feature dimension can significantly improve the model accuracy.

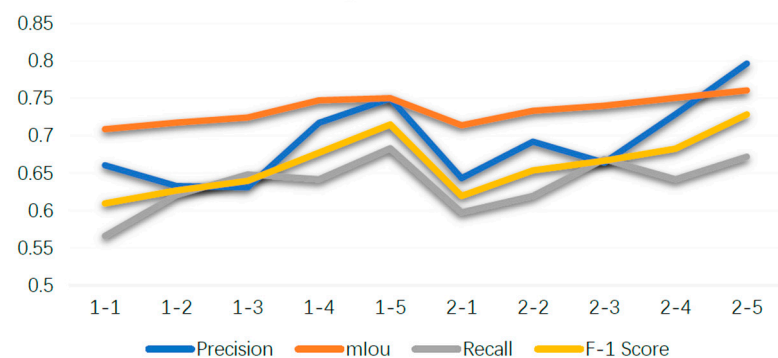
**Table 3.** List of experiments carried out in the study.

Experiment Number	Experiment			
	Feature Input		Model (Backbone Network)	Training Epochs
	Feature Selection	Number of Bands		
1-1	Image (RGB)	3	U-Net	50
1-2			DeepLab V3+ (ResNet18)	50
1-3			DeepLab V3+ (ResNet34)	50
1-4			DeepLab V3+ (ResNet50)	50
1-5			DeepLab V3+ (ResNet50)	100
2-1	Image (RGB) DEM Slope Aspect	6	U-Net	50
2-2			DeepLab V3+ (ResNet18)	50
2-3			DeepLab V3+ (ResNet34)	50
2-4			DeepLab V3+ (ResNet50)	50
2-5			DeepLab V3+ (ResNet50)	100

**Table 4.** Evaluation indicators of different experiments.

Num	Precision	mIou	Recall	F-1 Score
1-1	0.660389	0.708744	0.566244	0.609704
1-2	0.632827	0.717469	0.620872	0.626793
1-3	0.631112	0.724469	0.648415	0.639647
1-4	0.717093	0.747202	0.641909	0.677421
1-5	0.749731	0.750279	0.683364	0.715011
2-1	0.643282	0.713783	0.597672	0.619639
2-2	0.692092	0.73331	0.619586	0.653835
2-3	0.664166	0.740159	0.668856	0.666503
2-4	0.728748	0.750367	0.641902	0.682574
2-5	0.796203	0.760474	0.672002	0.728404

### Evaluation Indicators of Different Experiments

**Figure 10.** Evaluation indicators of different experiments.

With the above understanding, we focus on the qualitative comparison of the experimental results numbered “1-1”, “1-5”, “2-1”, and “2-5” in terms of missed and false judgments and spatial matching degree of recognition range. Figure 11 shows the identification results of the same earthquake landslide from four different model methods with experiment numbers of “1-1”, “1-5”, “2-1”, and “2-5”.

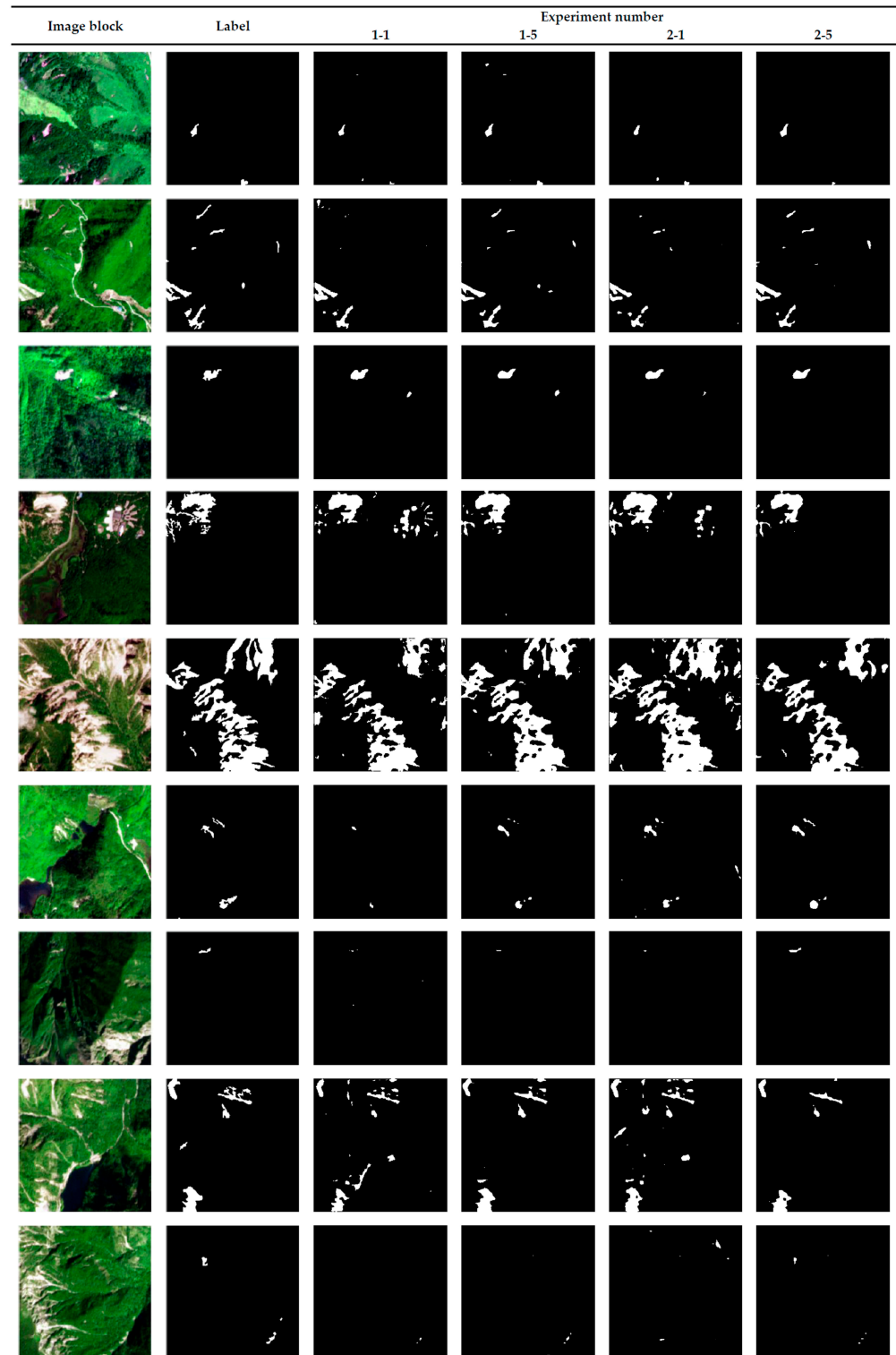


Figure 11. Comparison of prediction results of four main model methods.

We compared the qualitative results from two dimensions. First, when the feature inputs were consistent (both were single-feature inputs of optical images or multichannel spectral–topographic fusion features), DeepLab V3+ showed fewer false positives and a more accurate recognition range than U-Net. In particular, the experiment “2-5”, that is, the verification results of the embedded multichannel spectral–topographic feature fusion coseismic landslide extraction model proposed in this study, had a higher degree of discrimination for mixed pixels, better recognition results for landslide perimeter, and the rate of its misidentification of clouds as well as buildings, roads, and other ground objects was significantly lower than that of other methods. Second, compared with the single-feature input of an optical image, when multichannel spectral–topographic fusion feature was used as the feature input, whether U-Net or DeepLab V3+ was used, the model recognition results showed a better recognition effect. According to the verification results, experiment “2-1” was more accurate than experiment “1-1”; that is, the U-Net model with geosciences knowledge features was relatively more accurate in identifying the boundary. The slight spot noise was relatively reduced, but there were some missing judgments and misjudgments of roads and buildings, which are problematic for identifying large landslides. There were also non-Jiuzhaigou earthquake-triggered landslides. Compared with “1-5”, the landslide boundary identified by the DeepLab V3+ model with geoscientific knowledge features in experiment “2-5” was more accurate and smooth, with better connectivity. Cloud, building, and road misjudgments were less frequent than in other methods, which helped it to more accurately eliminate landslides not triggered by the Jiuzhaigou earthquake.

## 5. Discussion

### 5.1. The Importance of Multisource Data Feature Fusion

By comparing experimental results, it can be seen that integrating DEM, slope, aspect, and other known geological features related to the landslide is very helpful in improving the accuracy of landslide extraction. The multichannel spectral–topographic feature fusion model, which integrates geological knowledge and optical image features, increases the feature input dimensions related to landslides on the one hand, and on the other hand, through deeper backbone networks and training epochs, obtains a more generalized model for extracting coseismic landslides. As is shown in Figures 12 and 13, the multichannel spectral–topographic feature fusion model supported by multi feature data has better capability in boundary accuracy and missed or misjudged landslide identification results. Moreover, the addition of geosciences knowledge features has the effect of more reliably excluding buildings, roads, and other features that are easily misjudged as earthquake landslides. This is consistent with the research conclusions of [58,61] and other studies. Therefore, the increase in feature dimensions brought about by multisource data fusion related to the occurrence of coseismic landslides plays an important role in the identification accuracy of the model.

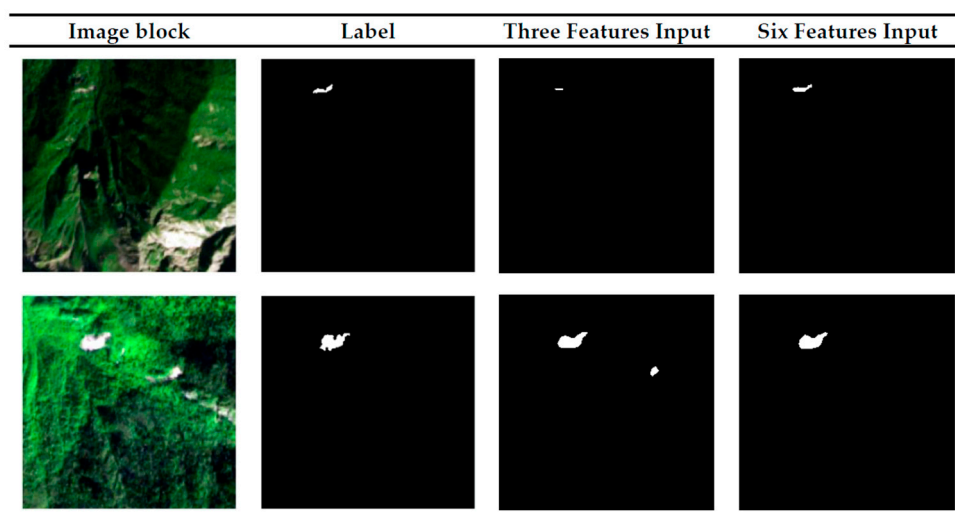


**Figure 12.** Comparison results of the same model for different input features.

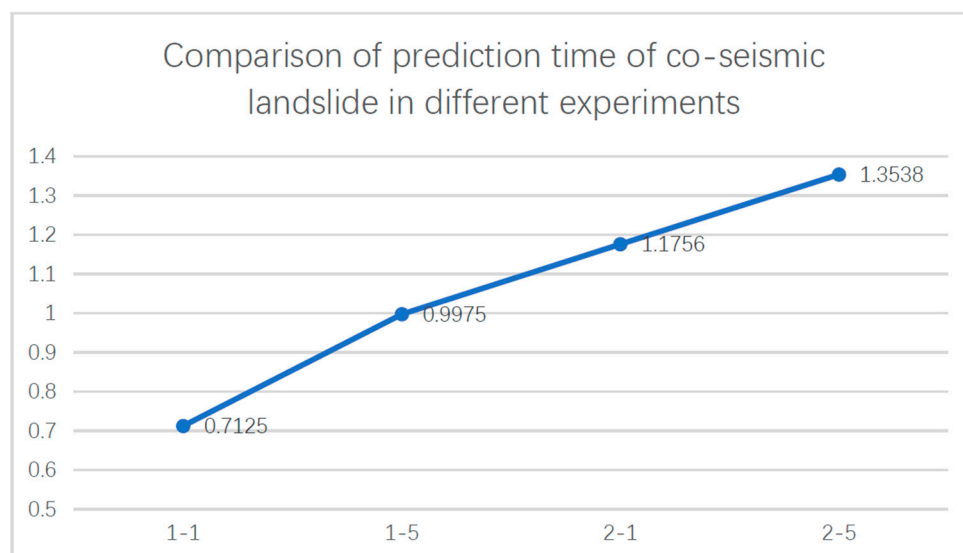


**Figure 13.** Comparison results of U-Net and DeepLab V3+ models under six-feature input.

### 5.2. Applicability of the Model for Earthquake Emergency Scenarios

After an earthquake, the extraction of coseismic landslides based on multisource data, such as multi temporal optical remote sensing images, DEM, and its derived data, is needed for the multichannel spectral–topographic feature fusion model. Therefore, the applicability of the post-earthquake coseismic landslide extraction model is largely constrained by the availability of data. The more data are required, the lower the availability. For example, in the case of the Jiuzhaigou earthquake, the weather conditions after the earthquake were poor, and the complete and available optical remote sensing image data for the earthquake area could not be obtained for a long time. This affected the timeliness of the landslide detection data acquisition and the response time of the earthquake emergency services. According to the quantitative and qualitative evaluation results of Section 4, the iterative extraction of coseismic landslide information can be continued by adjusting and supplementing the data input of the multichannel spectral–topographic feature fusion coseismic landslide extraction model following the order of post-earthquake data acquisition, enabling the provision of different levels of coseismic landslide extraction data at different times for the post-earthquake emergency.

Although we can improve the prediction efficiency of the model by image segmentation, the prediction efficiency of coseismic landslides will be different in different models

because of different data feature input dimensions and network depths. Figure 14 focuses on the time taken by four different models with experiment numbers “1-1”, “1-5”, “2-1”, and “2-5” to extract the coseismic landslide in the verification area of 142.5408 km<sup>2</sup> under the same hardware and software conditions. U-Net is slightly more efficient than DeepLab V3+ when feature inputs are consistent. For the same model, when the feature inputs are different, the feature inputs are positively correlated with the prediction time consumption. However, in general, the experiment time does not change significantly because of the increase in input features and network layers. Compared with simple models, the embedded multichannel spectral–topographic feature fusion model of coseismic landslide extraction shows no dramatic increase in computational complexity when extraction accuracy is improved. Therefore, in order to ensure the extraction accuracy of wide-area coseismic landslides, and on the premise that the timeliness of multisource data feature acquisition is guaranteed, the embedded multichannel spectral–topographic feature fusion model of wide-area coseismic landslide extraction can be preferentially selected for earthquake emergencies. However, when multisource data features are difficult to obtain because of poor weather after the earthquake, satellite transit time, and other reasons, the DeepLab V3+ with single-image feature input, that is, the model used for experiment No. 1-5 to extract the wide-area coseismic landslide in the earthquake area, is preferred.

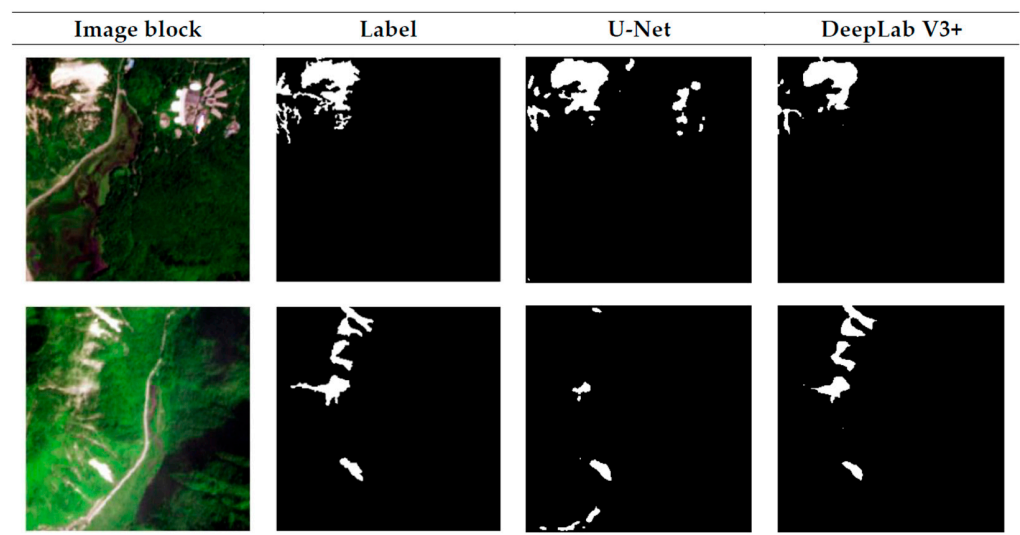


**Figure 14.** Comparison of coseismic landslide prediction time in different experiments.

## 6. Conclusions

Guided by post-earthquake emergency demands and taking coseismic landslides as the research object, this study proposed an embedded multichannel spectral–topographic feature fusion model for the rapid and accurate extraction of wide-area coseismic landslides that integrates geosciences knowledge and optical images. The model was mainly composed of three parts: embedded multichannel spectral–topographic feature fusion input, ResNet with cavity convolution, and encoder and decoder composed of atrous spatial pyramid pooling. Through the improvement and optimization of the network structure, the model effectively integrated the multiscale features and context information in the deep learning model while fully utilizing the optical image spectral and texture features of the coseismic landslide, as well as DEM, slope, aspect, and other topographic and geomorphic features. A knowledge-enhanced deep learning model for coseismic landslide extraction was constructed, integrating scientific knowledge of research objects. Because the model adopts separable depth convolution, it reduces the parameter sequence and ensures computational efficiency.

Based on the Jiuzhaigou earthquake coseismic landslide cataloging data in the study area, the comparison of the different model experiment results shows that, compared

with the coseismic landslide identification results of U-Net, DeepLab V3+, and other classic semantic segmentation networks, the embedded multichannel spectral–topographic feature fusion model for the rapid and accurate extraction of wide-area coseismic landslides proposed in this study integrates geological knowledge and optical images and realizes a more accurate identification, at both the quantitative and qualitative levels. In particular, the division of mixed pixels effectively alleviates the problem of missed or incorrectly judged coseismic landslides caused by complex scenes including features such as buildings, roads, cloud and snow cover, shadows, etc. The research shows that with a wide-area complex background, the coseismic landslide extraction model provides the following verified accuracy scores: Precision—0.796203; Recall—0.672002; F1 score—0.728404. This method realizes the accurate extraction of coseismic landslides in “big background and small target” scenes to a certain extent, greatly reduces labor costs, saves time, and can meet the needs of a post-earthquake emergency by obtaining timely, high-precision, and wide-area coseismic landslide data.

With the development of remote sensing technology, the abilities of multisource data support and information extraction has been improved. The deep learning method has replaced shallow features, such as spectral texture, with high-level semantic information, improving recognition accuracy. However, because the triggering conditions of coseismic landslides differ from those of other types of landslides, they often show irregular shapes caused by the impact of ground motion without obvious texture characteristics. Mixed pixels and background noise pose a serious problem. The high-precision extraction of coseismic landslides depends on high-quality and robust coseismic landslide data. In the future, the training dataset will be further expanded by integrating the scientific knowledge of the research object, including multisource remote sensing images, quantitative indexes, and topographic and geomorphological data, grounded in in-depth research on the triggering mechanisms of coseismic landslides, in order to build a better knowledge-enhanced deep learning model for coseismic landslide extraction.

**Author Contributions:** Conceptualization, X.Z., G.H. and L.H.; methodology, X.Z., G.H. and L.H.; validation, G.W. and L.F.; formal analysis, X.Z., L.H. and G.W.; data curation, L.F.; writing—original draft preparation, X.Z., L.H., L.F. and N.W.; writing—review and editing, X.Z. and G.H.; visualization, L.F. and N.W.; project administration, G.W. and L.F.; funding acquisition, G.H. All authors have read and agreed to the published version of the manuscript.

**Funding:** This research was funded by the Strategic Priority Research Program of the Chinese Academy of Sciences, grant number XDA19090300, the program of the National Natural Science Foundation of China, grant number 61731022, 61860206004 and the Second Tibetan Plateau Scientific Expedition and Research Program (STEP), grant number 2019QZKK030701.

**Data Availability Statement:** Not applicable.

**Acknowledgments:** The authors thank the anonymous reviewers and the editors for their valuable suggestions to improve our manuscript.

**Conflicts of Interest:** The authors declare no conflict of interest.

## References

1. Dai, L.X.; Xu, Q.; Fan, X.M.; Chang, M.; Yang, Q.; Yang, F.; Ren, J. A preliminary study on remote sensing interpretation of landslides triggered by earthquake in Sichuan on August 8th, 2017 and their spatial distribution patterns. *J. Eng. Geol.* **2017**, *25*, 1151–1164.
2. Peng, L.; Xu, S.N.; Mei, J.J.; Su, F.H. Earthquake-induced landslide recognition using high-resolution remote sensing images. *J. Remote Sens.* **2017**, *21*, 509–518. [[CrossRef](#)]
3. Bischof, H.; Schneider, W.; Pinz, A.J. Multispectral classification of Landsat-images using neural networks. *IEEE Trans. Geosci. Remote Sens.* **1992**, *30*, 482–490. [[CrossRef](#)]
4. Barlow, J.; Martin, Y.; Franklin, S.E. Detecting translational landslide scars using segmentation of Landsat ETM+ and DEM data in the northern Cascade Mountains, British Columbia. *Can. J. Remote Sens.* **2003**, *29*, 510–517. [[CrossRef](#)]
5. Nichol, J.; Wong, M.S. Satellite remote sensing for detailed landslide inventories using change detection and image fusion. *Int. J. Remote Sens.* **2005**, *26*, 1913–1926. [[CrossRef](#)]

6. Hua, L.Z.; Cui, S.H.; Li, X.H.; Yin, K.; Qiu, Q.Y. Remote sensing identification of earthquake triggered landslides and their impacts on ecosystem services: A case study of Wenchuan County. *Acta Ecol. Sin.* **2008**, *28*, 5909–5916.
7. Rosin, P.L.; Hervás, J. Remote sensing image thresholding methods for determining landslide activity. *Int. J. Remote Sens.* **2005**, *26*, 1075–1092. [[CrossRef](#)]
8. Borghuis, A.M.; Chang, K.; Lee, H.Y. Comparison between automated and manual mapping of typhoon-triggered landslides from SPOT-5 imagery. *Int. J. Remote Sens.* **2007**, *28*, 1843–1856. [[CrossRef](#)]
9. Su, F.H.; Liu, H.J.; Han, Y.S. The extraction of mountain hazard induced by wenchuan earthquake and analysis of its distributing characteristic. *J. Remote Sens.* **2008**, *12*, 956–963. [[CrossRef](#)]
10. Yang, X.J.; Chen, L.D. Using multi-temporal remote sensor imagery to detect earthquake-triggered landslides. *Int. J. Appl. Earth Obs. Geoinf.* **2010**, *12*, 487–495. [[CrossRef](#)]
11. Zhang, W.J.; Lin, J.Y.; Peng, J.; Lu, Q.F. Estimating Wenchuan Earthquake induced landslides based on remote sensing. *Int. J. Remote Sens.* **2010**, *31*, 3495–3508. [[CrossRef](#)]
12. Zhao, W.; Li, A.N.; Nan, X.; Zhang, Z.J.; Lei, G.B. Post-earthquake landslides mapping from Landsat-8 data for the 2015 Nepal Earthquake using a pixel-based change detection method. *IEEE J. Sel. Top. Appl. Earth Obs. Remote Sens.* **2017**, *10*, 1758–1768. [[CrossRef](#)]
13. Ramos-Bernal, R.N.; Vázquez-Jiménez, R.; Romero-Calcerrada, R.; Arrogante-Funes, P.; Novillo, C.J. Evaluation of Unsupervised Change Detection Methods Applied to Landslide Inventory Mapping Using ASTER Imagery. *Remote Sens.* **2018**, *10*, 1987. [[CrossRef](#)]
14. Lei, T.; Xue, D.; Lv, Z.; Li, S.; Zhang, Y.K.; Nandi, A. Unsupervised Change Detection Using Fast Fuzzy Clustering for Landslide Mapping from Very High-Resolution Images. *Remote Sens.* **2018**, *10*, 1381. [[CrossRef](#)]
15. Miura, T.; Nagai, S. Landslide Detection with Himawari-8 Geostationary Satellite Data: A Case Study of a Torrential Rain Event in Kyushu, Japan. *Remote Sens.* **2020**, *12*, 1734. [[CrossRef](#)]
16. He, G.J.; Zhang, Z.M.; Jiao, W.L.; Long, T.F.; Peng, Y.; Wang, G.Z.; Yin, R.Y.; Wang, W.; Zhang, X.M.; Liu, H.C.; et al. Generation of ready to use (RTU) products over China based on Landsat series data. *Big Earth Data* **2018**, *2*, 56–64. [[CrossRef](#)]
17. Li, Y. Research on Landslide Detection Algorithm Based on Deep Learning. Chengdu University of Technology, Chengdu, China, 2018.
18. Ghorbanzadeh, O.; Blaschke, T.; Gholamnia, K.; Meena, S.R.; Tiede, D.; Aryal, J. Evaluation of Different Machine Learning Methods and Deep-Learning Convolutional Neural Networks for Landslide Detection. *Remote Sens.* **2019**, *11*, 196. [[CrossRef](#)]
19. Tavakkoli Piralilou, S.; Shahabi, H.; Jarhani, B.; Ghorbanzadeh, O.; Blaschke, T.; Gholamnia, K.; Meena, S.R.; Aryal, J. Landslide Detection Using Multi-Scale Image Segmentation and Different Machine Learning Models in the Higher Himalayas. *Remote Sens.* **2019**, *11*, 2575. [[CrossRef](#)]
20. Shirvani, Z.; Abdi, O.; Buchroithner, M. A Synergetic Analysis of Sentinel-1 and -2 for Mapping Historical Landslides Using Object-Oriented Random Forest in the Hyrcanian Forests. *Remote Sens.* **2019**, *11*, 2300. [[CrossRef](#)]
21. Liang, R.; Dai, K.; Shi, X.; Guo, B.; Dong, X.; Liang, F.; Tomás, R.; Wen, N.; Fan, X. Automated Mapping of Ms 7.0 Jiuzhaigou Earthquake (China) Post-Disaster Landslides Based on High-Resolution UAV Imagery. *Remote Sens.* **2021**, *13*, 1330. [[CrossRef](#)]
22. He, G.J.; Wang, L.Z.; Ma, Y.; Zhang, Z.M.; Wang, G.Z.; Peng, Y.; Long, T.F.; Zhang, X.M. Processing of earth observation big data: Challenges and countermeasures. *Chin. Sci. Bull.* **2015**, *60*, 470–478. (In Chinese) [[CrossRef](#)]
23. Lobo, A.; Chic, O.; Casterad, A. Classification of Mediterranean crops with multi-sensor data: Per-pixel versus per-object statistics and image segmentation. *Int. J. Remote Sens.* **1996**, *17*, 2385–2400. [[CrossRef](#)]
24. Baatz, M.; Schäpe, A. Object-oriented and multi-scale image analysis in semantic networks. In Proceedings of the Second International Symposium on Operationalization of Remote Sensing, Enschede, The Netherlands, 16–20 August 1999; pp. 2563–2575.
25. Mauro, C.; Eufemia, T. Accuracy assessment of Per-field classification integrating very fine spatial resolution satellite imagery with topographic data. *J. Geospat. Eng.* **2001**, *3*, 127–134.
26. Giada, S.; De Groeve, T.; Ehrlich, D.; Soille, P. Information extraction from very high resolution satellite imagery over Lukole refugee camp, Tanzania. *Int. J. Remote Sens.* **2003**, *24*, 4251–4266. [[CrossRef](#)]
27. Huang, H.P.; Wu, B.F.; Fan, J.L. Analysis to the relationship of classification accuracy, segmentation scale, image resolution. In Proceedings of the 2003 IEEE International Geoscience and Remote Sensing Symposium, Toulouse, France, 21–25 July 2003; IEEE: Piscataway, NJ, USA, 2003; pp. 3671–3673. [[CrossRef](#)]
28. Hu, D.Y.; Li, J.; Zhao, W.J.; Peng, G.X. Object-oriented landslide detection from remote sensing imageries with high resolution. *J. Nat. Disasters* **2008**, *17*, 42–46. [[CrossRef](#)]
29. Ren, Y.H.; Liu, Y.L.; Wei, C.J.; Hu, L.Q. Study on information extraction method to road damage in Wenchuan earthquake based on high-resolution remote sensing images. *Remote Sens. Technol. Appl.* **2009**, *24*, 52–56. [[CrossRef](#)]
30. Niu, Q.F.; Cheng, W.M.; Lan, H.X.; Liu, Y.; Xie, Y.W.; Cao, Y.Y. The extraction of landslide hazard induced by Yushu earthquake and analysis of its distributing characteristic. In Proceedings of the Symposium on Emergency Handling and Disaster Prevention and Control Technology for Sudden Geological Disasters in China, Lanzhou, China, 25–27 June 2010; pp. 39–45.
31. Chen, T.B.; Hu, Z.W.; Wei, L.; Hu, S.Q. Data processing and landslide information extraction based on UAV remote sensing. *J. Geo-Inf. Sci.* **2017**, *19*, 692–701.
32. Lu, P.; Stumpf, A.; Kerle, N.; Casagli, N. Object-oriented change detection for landslide rapid mapping. *IEEE Geosci. Remote Sens. Lett.* **2011**, *8*, 701–705. [[CrossRef](#)]

33. Stumpf, A.; Kerle, N. Object-oriented mapping of landslides using Random Forests. *Remote Sens. Environ.* **2011**, *115*, 2564–2577. [[CrossRef](#)]
34. Ding, H.; Zhang, M.S.; Li, L. Regional landslide identification base on Multi-feature Object-oriented image classification. *Remote Sens. Technol. Appl.* **2013**, *28*, 1107–1113.
35. Zhang, Y.; Tan, L.; Chen, G.; Guo, P.; Qiao, L.; Meng, X.M. Landslide information extracted from high resolution remote sensing based on the object oriented classification method. *J. Lanzhou Univ. (Nat. Sci.)* **2014**, *50*, 745–750. [[CrossRef](#)]
36. Blaschke, T.; Feizizadeh, B.; Holbling, D. Object-based image analysis and digital terrain analysis for locating landslides in the Urmia Lake basin, Iran. *IEEE J. Sel. Top. Appl. Earth Obs. Remote Sens.* **2014**, *7*, 4806–4817. [[CrossRef](#)]
37. Kurtz, C.; Stumpf, A.; Malet, J.P.; Gañarski, P.; Puissant, A.; Passat, N. Hierarchical extraction of landslides from multiresolution remotely sensed optical images. *ISPRS J. Photogramm. Remote Sens.* **2014**, *87*, 122–136. [[CrossRef](#)]
38. Rau, J.Y.; Jhan, J.P.; Rau, R.J. Semiautomatic object-oriented landslide recognition scheme from multi-sensor optical imagery and DEM. *IEEE Trans. Geosci. Remote Sens.* **2014**, *52*, 1336–1349. [[CrossRef](#)]
39. Dou, J.; Chang, K.T.; Chen, S.S.; Yunus, A.P.; Liu, J.K.; Xia, H.; Zhu, Z.F. Automatic case-based reasoning approach for landslide detection: Integration of object-oriented image analysis and a genetic algorithm. *Remote Sens.* **2015**, *7*, 4318–4342. [[CrossRef](#)]
40. Hölbling, D.; Friedl, B.; Eisank, C. An object-based approach for semi-automated landslide change detection and attribution of changes to landslide classes in northern Taiwan. *Earth Sci. Inform.* **2015**, *8*, 327–335. [[CrossRef](#)]
41. Martha, T.R.; Kamala, P.; Jose, J.; Kumar, K.V.; Sankar, G.J. Identification of new landslides from high resolution satellite data covering a large area using object-based change detection methods. *J. Indian Soc. Remote Sens.* **2016**, *44*, 515–524. [[CrossRef](#)]
42. Martha, T.R.; Kerle, N.; Jetten, V.; Van Westen, C.J.; Kumar, K.V. Characterising spectral, spatial and morphometric properties of landslides for semi-automatic detection using object-oriented methods. *Geomorphology* **2010**, *116*, 24–36. [[CrossRef](#)]
43. Martha, T.R.; Kerle, N.; Van Westen, C.J.; Jetten, V.; Kumar, K.V. Object-oriented analysis of multi-temporal panchromatic images for creation of historical landslide inventories. *ISPRS J. Photogramm. Remote Sens.* **2012**, *67*, 105–119. [[CrossRef](#)]
44. Li, Z.B.; Shi, W.Z.; Lu, P.; Wang, Q.M.; Miao, Z.L. Landslide mapping from aerial photographs using change detection-based Markov random field. *Remote Sens. Environ.* **2016**, *187*, 76–90. [[CrossRef](#)]
45. Kamps, M.; Bouten, W.; Seijmonsbergen, A.C. LiDAR and Orthophoto Synergy to optimize Object-Based Landscape Change: Analysis of an Active Landslide. *Remote Sens.* **2017**, *9*, 805. [[CrossRef](#)]
46. Yan, Q. *Study on Rapid and Intelligent Extraction of Typical Seismic Secondary Geological Disasters Using High Resolution Remote Sensing Imagery*; Institute of Remote Sensing and Digital Earth, Chinese Academy of Sciences: Beijing, China, 2017.
47. Mezaal, M.R.; Pradhan, B.; Rizeei, H.M. Improving Landslide Detection from Airborne Laser Scanning Data Using Optimized Dempster-Shafer. *Remote Sens.* **2018**, *10*, 1029. [[CrossRef](#)]
48. Pawłuszek, K.; Marczak, S.; Borkowski, A.; Tarolli, P. Multi-Aspect Analysis of Object-Oriented Landslide Detection Based on an Extended Set of LiDAR-Derived Terrain Features. *ISPRS Int. J. Geo-Inf.* **2019**, *8*, 321. [[CrossRef](#)]
49. Li, Q.; Zhang, J.F.; Luo, Y.; Jiao, Q.S. Recognition of earthquake-induced landslide and spatial distribution patterns triggered by the Jiuzhaigou earthquake in August 8, 2017. *J. Remote Sens.* **2019**, *23*, 785–795. [[CrossRef](#)]
50. Li, Q.L.; Zhang, W.C.; Yi, Y.N. An information extraction method of earthquake-induced landslide: A case study of the Jiuzhaigou earthquake in 2017. *J. Univ. Chin. Acad. Sci.* **2020**, *37*, 93–102.
51. Karantanellis, E.; Marinos, V.; Vassilakis, E.; Christaras, B. Object-Based Analysis Using Unmanned Aerial Vehicles (UAVs) for Site-Specific Landslide Assessment. *Remote Sens.* **2020**, *12*, 1711. [[CrossRef](#)]
52. Lin, S.Y.; Lin, C.W.; van Gasselt, S. Processing Framework for Landslide Detection Based on Synthetic Aperture Radar (SAR) Intensity-Image Analysis. *Remote Sens.* **2021**, *13*, 644. [[CrossRef](#)]
53. Han, Y.; Wang, P.; Zheng, Y.; Yasir, M.; Xu, C.; Nazir, S.; Hossain, M.S.; Ullah, S.; Khan, S. Extraction of Landslide Information Based on Object-Oriented Approach and Cause Analysis in Shuicheng, China. *Remote Sens.* **2022**, *14*, 502. [[CrossRef](#)]
54. Liu, Y.; Wu, L.Z. Geological Disaster Recognition on Optical Remote Sensing Images Using Deep Learning. *Procedia Comput. Sci.* **2016**, *91*, 566–575. [[CrossRef](#)]
55. Recep, C.; Sultan, K.; Candan, G. A Convolutional Neural Network Architecture for Auto-Detection of Landslide Photographs to Assess Citizen Science and Volunteered Geographic Information Data Quality. *ISPRS Int. J. Geo-Inf.* **2019**, *8*, 300.
56. Wang, Y.; Wang, X.F.; Jian, J.F. Remote Sensing Landslide Recognition Based on Convolutional Neural Network. *Math. Probl. Eng.* **2019**, 11–12. [[CrossRef](#)]
57. Wang, Y.; Yang, Y.; Wang, B.S.; Wang, T.; Bu, X.H.; Wang, C.Y. Building segmentation in high high-resolution remote sensing image through deep neural network and conditional random fields. *J. Remote Sens.* **2019**, *23*, 1194–1208.
58. Liu, P.; Wei, Y.M.; Wang, Q.J.; Chen, Y.; Xie, J.J. Research on Post-Earthquake Landslide Extraction Algorithm Based on Improved U-Net Model. *Remote Sens.* **2020**, *12*, 894. [[CrossRef](#)]
59. Xu, B.Z. Landslide Range Extraction from UAV Images Based on Multiscale Depth Attention Model and It's Application in Susceptibility Assessment. Southwest Jiaotong University, Chengdu, China, 2020.
60. Prakash, N.; Manconi, A.; Loew, S. Mapping Landslides on EO Data: Performance of Deep Learning Models vs. Traditional Machine Learning Models. *Remote Sens.* **2020**, *12*, 346. [[CrossRef](#)]
61. Xia, W.; Chen, J.; Liu, J.; Ma, C.; Liu, W. Landslide Extraction from High-Resolution Remote Sensing Imagery Using Fully Convolutional Spectral-Topographic Fusion Network. *Remote Sens.* **2021**, *13*, 5116. [[CrossRef](#)]

62. Shahabi, H.; Rahimzad, M.; Tavakkoli Piralilou, S.; Ghorbanzadeh, O.; Homayouni, S.; Blaschke, T.; Lim, S.; Ghamisi, P. Unsupervised Deep Learning for Landslide Detection from Multispectral Sentinel-2 Imagery. *Remote Sens.* **2021**, *13*, 4698. [[CrossRef](#)]
63. Yu, B.; Chen, F.; Xu, C.; Wang, L.; Wang, N. Matrix SegNet: A Practical Deep Learning Framework for Landslide Mapping from Images of Different Areas with Different Spatial Resolutions. *Remote Sens.* **2021**, *13*, 3158. [[CrossRef](#)]
64. Zhang, X.; Pun, M.O.; Liu, M. Semi-Supervised Multi-Temporal Deep Representation Fusion Network for Landslide Mapping from Aerial Orthophotos. *Remote Sens.* **2021**, *13*, 548. [[CrossRef](#)]
65. Plank, S.; Twele, A.; Martinis, S. Landslide Mapping in Vegetated Areas Using Change Detection Based on Optical and Polarimetric SAR Data. *Remote Sens.* **2016**, *8*, 307. [[CrossRef](#)]
66. Burrows, K.; Walters, R.J.; Milledge, D.; Spaans, K.; Densmore, A.L. A New Method for Large-Scale Landslide Classification from Satellite Radar. *Remote Sens.* **2019**, *11*, 237. [[CrossRef](#)]
67. Mondini, A.C.; Santangelo, M.; Rocchetti, M.; Rossetto, E.; Manconi, A.; Monserrat, O. Sentinel-1 SAR Amplitude Imagery for Rapid Landslide Detection. *Remote Sens.* **2019**, *11*, 760. [[CrossRef](#)]
68. Aimaiti, Y.; Liu, W.; Yamazaki, F.; Maruyama, Y. Earthquake-Induced Landslide Mapping for the 2018 Hokkaido Eastern Iburi Earthquake Using PALSAR-2 Data. *Remote Sens.* **2019**, *11*, 2351. [[CrossRef](#)]
69. Jung, J.; Yun, S.H. Evaluation of Coherent and Incoherent Landslide Detection Methods Based on Synthetic Aperture Radar for Rapid Response: A Case Study for the 2018 Hokkaido Landslides. *Remote Sens.* **2020**, *12*, 265. [[CrossRef](#)]
70. Li, Z.; Li, S.S.; Ge, X.Q. Transfer learning method to extract landslide after the Wenchuan earthquake of GF-1 image. *J. Remote Sens.* **2021**. [[CrossRef](#)]
71. Ye, R.Q.; Deng, Q.L.; Wang, H.Q. Landslide Identification Based on Image Classification: A Case Study on Guizhoulaocheng landslide in the Three Gorges Reservoir Area. *Chin. J. Eng. Geophys.* **2007**, *4*, 574–577. [[CrossRef](#)]
72. Li, Y.; Cui, P.; Ye, C.; Junior, J.M.; Zhang, Z.; Guo, J.; Li, J. Accurate Prediction of Earthquake-Induced Landslides Based on Deep Learning Considering Landslide Source Area. *Remote Sens.* **2021**, *13*, 3436. [[CrossRef](#)]
73. Huang, R.Q.; Li, W.L. Research on Development and Distribution Rules of Geohazards Induced by Wenchuan Earthquake on 12<sup>th</sup> May, 2008. *Chin. J. Rock Mech. Eng.* **2008**, *27*, 2585–2592.
74. Chen, L.C.; Zhu, Y.; Papandreou, G.; Schroff, F.; Adam, H. Encoder-Decoder with Atrous Separable Convolution for Semantic Image Segmentation. In Proceedings of the Computer Vision—ECCV 2018, Munich, Germany, 8–14 September 2018.
75. He, K.; Zhang, X.; Ren, S.; Sun, J. Deep Residual Learning for Image Recognition. In Proceedings of the 2016 IEEE Conference on Computer Vision and Pattern Recognition (CVPR), Las Vegas, NV, USA, 27–30 June 2016; pp. 770–778. [[CrossRef](#)]
76. Chen, L.C.; Papandreou, G.; Schroff, F.; Adam, H. Rethinking Atrous Convolution for Semantic Image Segmentation. *arXiv* **2017**. [[CrossRef](#)]
77. Fu, G.C.; Li, T.Y.; Sun, D.X.; Xiong, R.W. Seismogenic Structure of The Ms7.0 Earthquake on August 8, 2017 in JiuZhaiGou, SiChuan. *J. Geomech.* **2017**, *23*, 799–809.
78. Chen, X.L.; Shan, X.J.; Zhang, L.; Liu, C.G.; Han, N.N.; Lan, J. Quick assessment of earthquake-triggered landslide hazards: A case study of the 2017 Ms7.0 Jiuzhaigou earthquake. *Erath Sci. Front.* **2019**, *26*, 312–320. [[CrossRef](#)]
79. Bruneau, M.; Chang, S.E.; Eguchi, R.T.; Lee, G.C.; O'Rourke, T.D.; Reinhorn, A.M.; Shinozuka, M.; Tierney, K.; Wallace, W.A.; Von Winterfeldt, D. A Framework to Quantitatively Assess and Enhance the Seismic Resilience of Communities. *Earthq. Spectra* **2003**, *19*, 733–752. [[CrossRef](#)]
80. Elms, D.G. Improving Community Resilience to Natural Events. *Civ. Eng. Environ. Syst.* **2015**, *32*, 77–89. [[CrossRef](#)]
81. Forcellini, D. A resilience-based methodology to assess soil structure interaction on a benchmark bridge. *Infrastructures* **2020**, *5*, 90. [[CrossRef](#)]
82. Forcellini, D. A new methodology to assess indirect losses in bridges subjected to multiple hazards. *Innov. Infrastruct. Solut.* **2019**, *4*, 10. [[CrossRef](#)]
83. Zhai, C.; Zhao, Y.; Wen, W.; Qin, H.; Xie, L. A novel urban seismic resilience assessment method considering the weighting of post-earthquake loss and recovery time. *Int. J. Disaster Risk Reduct.* **2023**, *84*, 103453. [[CrossRef](#)]
84. Dong, X.J.; Xu, Q.; She, J.X.; Li, W.L.; Liu, F.; Zhou, X.X. Preliminary Study on Interpretation of Geological Hazards in Jiuzhaigou Based on Multi-source Remote Sensing Data. *Geomat. Inf. Sci. Wuhan Univ.* **2020**, *45*, 432–441. [[CrossRef](#)]
85. Xu, X.W.; Chen, G.H.; Wang, Q.X.; Chen, L.C.; Ren, Z.K.; Xu, C.; Wei, Z.Y.; Lu, R.Q.; Tan, X.B.; Dong, S.P.; et al. Discussion on seismogenic structure of Jiuzhaigou earthquake and its implication for current strain state in the southeastern Qinghai-Tibet plateau. *Chin. J. Geophys.* **2017**, *60*, 4018–4026. [[CrossRef](#)]

**Disclaimer/Publisher's Note:** The statements, opinions and data contained in all publications are solely those of the individual author(s) and contributor(s) and not of MDPI and/or the editor(s). MDPI and/or the editor(s) disclaim responsibility for any injury to people or property resulting from any ideas, methods, instructions or products referred to in the content.